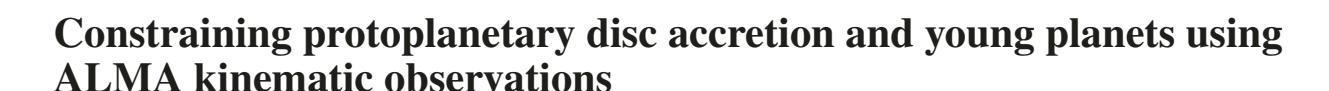
doi:10.1093/mnras/stab447



Ian Rabago <sup>®</sup>★ and Zhaohuan Zhu <sup>®</sup>

Department of Physics and Astronomy, University of Nevada, Las Vegas 4505 S. Maryland Parkway Las Vegas, NV 89154, USA

Accepted 2021 February 9. Received 2021 January 27; in original form 2020 November 17

#### **ABSTRACT**

Recent ALMA molecular line observations have revealed 3D gas velocity structure in protoplanetary discs, shedding light on mechanisms of disc accretion and structure formation. (1) By carrying out viscous simulations, we confirm that the disc's velocity structure differs dramatically using vertical stress profiles from different accretion mechanisms. Thus, kinematic observations tracing flows at different disc heights can potentially distinguish different accretion mechanisms. On the other hand, the disc surface density evolution is mostly determined by the vertically integrated stress. The sharp disc outer edge constrained by recent kinematic observations can be caused by a radially varying  $\alpha$  in the disc. (2) We also study kinematic signatures of a young planet by carrying out 3D planet—disc simulations. The relationship between the planet mass and the 'kink' velocity is derived, showing a linear relationship with little dependence on disc viscosity, but some dependence on disc height when the planet is massive (e.g.  $10M_J$ ). We predict the 'kink' velocities for the potential planets in DSHARP discs. At the gap edge, the azimuthally averaged velocities at different disc heights deviate from the Keplerian velocity at similar amplitudes, and its relationship with the planet mass is consistent with that in 2D simulations. After removing the planet, the azimuthally averaged velocity barely changes within the viscous time-scale, and thus the azimuthally averaged velocity structure at the gap edge is due to the gap itself and not directly caused to the planet. Combining both axisymmetric kinematic observations and the residual 'kink' velocity is needed to probe young planets in protoplanetary discs.

**Key words:** accretion, accretion discs – astroparticle physics – dynamo – instabilities – MHD – turbulence.

## 1 INTRODUCTION

Protoplanetary discs are thought to be the sites of planetary formation. In recent years, use of ground-based radio telescopes such as the Atacama Large Millimeter Array (ALMA) has improved our ability to resolve protoplanetary discs, revealing a wealth of structure in many existing discs, including rings, spirals, and other non-axisymmetric structures (e.g. ALMA Partnership et al. 2015; Andrews et al. 2016, 2018). It is often suggested that the dark annular features observed in the dust continuum are gaps created by protoplanets as they repel material away from the planet (e.g. review by Espaillat et al. 2014; Andrews 2020). Despite the high frequency of gaps observed in high-resolution imagery, only a small number of forming planets have been discovered to date. One notable protoplanetary system is the disc of PDS 70, which contains two planetary-mass point sources detected by direct observation (Keppler et al. 2018; Wagner et al. 2018; Christiaens et al. 2019; Haffert et al. 2019; Isella et al. 2019; Wang et al. 2020). Many other discs have been suspected to contain protoplanets due to the presence of gaps and spirals within the disc, but there is much debate over their existence as these features are not a unique signature of planetary formation (e.g. Follette et al. 2017; Rameau et al. 2017; Brittain, Najita & Carr 2019; Cugno et al. 2019).

Besides planets, there are many other mechanisms that are able to form gaps in protoplanetary discs. Gaps and other axisymmetric structures can be formed by condensation of materials at snow lines (Zhang, Blake & Bergin 2015; Okuzumi et al. 2016), interaction of the disc material with magnetic fields (Kretke & Lin 2007; Johansen, Youdin & Klahr 2009; Bai & Stone 2014; Suriano et al. 2017; Hu et al. 2019, 2020), dust–gas secular gravitational instability (Takahashi & Inutsuka 2014; Tominaga, Takahashi & Inutsuka 2020), and indirectly from the spiral arm generated by a planet orbiting at a different radius (Bae, Zhu & Hartmann 2017; Dong et al. 2017). Determining which of the observed gaps are hosts to potential planets is an ongoing process and an area of active research.

Thanks to ALMA's high sensitivity to molecular lines, subthermal kinematic motion in protoplanetary discs can be probed using molecular lines, and such kinematic information provides more direct evidence of the planets in discs (Pinte et al. 2018; Teague et al. 2018). To extract the disc kinematic information from molecular lines, two different methods have been developed. Pinte et al. (2018) uses the high spectral-resolution channel maps to probe the disc region whose velocity structure is significantly disturbed by the planet. Such a non-axisymmetric disturbance is due to the horseshoe and circumplanetary motion around the planet (Perez et al. 2015; Pérez, Casassus & Benítez-Llambay 2018), forming a 'kink' in the channel maps. The second method, used by Teague et al. (2018), assumes that the disc flow is mostly axisymmetric, allowing the axisymmetric flow velocity to be calculated by averaging the

<sup>\*</sup> E-mail: rabagoi@unlv.nevada.edu

# 5326 I. Rabago and Z. Zhu

kinematic information along the disc's azimuthal direction. With this averaging process, sub-thermal axisymmetric deviations from the Keplerian motion can be extracted. Teague et al. (2018) analysed the rotational velocity structure in the gaps of disc HD 163296 and found that the super-Keplerian and sub-Keplerian rotational velocity at the gap edges could be explained by planets of  $1M_J$  at 100 AU and  $1.3M_J$  at 165 AU. A later work (Teague, Bae & Bergin 2019) examines the 2D velocity components of HD 163296, and finds evidence of meridional flows in the atmosphere above the gaps. Such meridional flow also resembles the flow structure in 3D planet—disc interaction simulations (Fung & Chiang 2016).

The relationship between the planet and the 'kink' velocity has not been derived. Pinte et al. (2018, 2019) derived the planet mass by comparing the observed channel maps with synthetic channel maps from direct numerical simulations. Although such an approach provides a more robust estimate on the planet mass, it is time consuming and computationally expensive for a large sample of discs (e.g. Pinte et al. 2020).

The relationship between the axisymmetric deviation from the Keplerian motion at the gap edge and the embedded planet mass has been derived in Zhang et al. (2018) and Gyeol Yun et al. (2019) using a grid of  $R - \phi$  2D simulations. However, strong molecular lines are normally produced at the disc surface which cannot be studied using  $R - \phi$  2D simulations. Thus, it is unclear if such derived relationships can be applied to real molecular line observations.

Besides probing the planet, the disc's axisymmetric deviation from the Keplerian velocity has also been used to study gaseous rings (Rosotti et al. 2020) and the disc's outer edge (Dullemond et al. 2020). Assuming that such velocity deviation is due to the radial pressure gradient in the disc, Dullemond et al. (2020) find that the disc around HD 163296 has a rather abrupt outer edge with  $\Sigma \propto \exp(-(R/R_d)^2)$ . Dullemond et al. (2020) suggest that it is due to outside-in photoevaporation or truncation by an unseen companion. On the other hand, the sharp outer edge could be due to the disc evolution itself, as we will argue in Section 4.1.

In this paper, we use 3D viscous simulations to study the relationship between the planet mass and the disc's 3D velocity structure (both the 'kink' velocity and the axisymmetric deviation from the Keplerain velocity at the gap edge). We also explore how probing the velocity structure could differentiate different accretion processes in protoplanetary discs. The disc could have complicated flow structure (e.g. meridional flow) even without gaps (Urpin 1984; Kley & Lin 1992; Rozyczka, Bodenheimer & Bell 1994). We will address how such flow pattern is related to the stress distribution in the disc, and how the disc surface density evolution depends on the stress distribution. Finally, we study the differences between the velocity structure of a gap which has a planet in it and that of a gap without a planet. In Section 2, we outline the viscous theory important to this work. We describe our simulation setup in Section 3, and present our results in Section 4. We discuss important results and implications of our findings in Section 5. Finally, we conclude in Section 6.

## 2 VISCOUS THEORY

Before we carry out viscous simulations for planet–disc interaction, we will first study the evolution of viscous discs without planets for two reasons. First, there is a well-developed analytical theory on viscous disc structure/evolution, which can be used to test the viscosity module for our numerical simulations. Secondly, by modifying the traditional viscous disc theory, we can derive the flow structure of discs undergoing different instabilities, and how

kinematic observations may be able to constrain these different accretion mechanisms.

In this section, a few analytical results from the viscous disc theory are reviewed, starting from 1D surface density evolution to 2D meridional circulation. Various stress profiles have been adopted to mimic the turbulent structure in discs subject to different disc instabilities. Then, motivated by some recent MHD simulations showing that the disc mostly accretes in the radial direction under the spherical polar coordinate system, we analytically derive the meridional circulation pattern under the spherical polar coordinate system. This new analytical derivation can also be compared with our spherical polar simulations more directly in Section 3.

#### 2.1 1D disc evolution

If the viscous disc has an internal viscosity of  $\nu$ , the disc's surface density  $(\Sigma)$  follows the diffusion equation

$$\frac{\partial \Sigma}{\partial t} = \frac{3}{R} \frac{\partial}{\partial R} \left[ R^{\frac{1}{2}} \frac{\partial}{\partial R} (R^{\frac{1}{2}} \nu \Sigma) \right]. \tag{1}$$

The analytical solution of this equation has been derived in Lynden–Bell & Pringle (1974). For a Keplerian disc with

$$\nu \propto R^{\gamma}$$
, (2)

one similarity solution is (we adopt the derivation from Hartmann et al. 1998)

$$\Sigma(r,t) = \frac{C}{3\pi\nu} T^{-\frac{5/2-\gamma}{2-\gamma}} \exp\left(\frac{-(R/R_1)^{2-\gamma}}{T}\right)$$
(3)

$$\dot{M}(r,t) = CT^{-\frac{5/2-\gamma}{2-\gamma}} \exp\left(\frac{-(R/R_1)^{2-\gamma}}{T}\right)$$

$$\times \left[ 1 - \frac{2(2-\gamma)(R/R_1)^{2-\gamma}}{T} \right] \tag{4}$$

with  $T = t/t_s + 1$ , where the viscous time-scale is

$$t_s = \frac{1}{3(2-\nu)^2} \frac{R_1^2}{\nu_1},\tag{5}$$

where  $v_1 = v(R_1)$ . The scaling factors for the surface density, radius, and time in this similarity solution are C,  $R_1$ , and  $t_s$ , respectively. Note that the surface density profile at one specific time follows

$$\Sigma(R) \propto \nu^{-1} \exp(-(R/R_2)^{2-\gamma}) \propto R^{-\gamma} \exp(-(R/R_2)^{2-\gamma}),$$
 (6)

where  $R_2 = R_1 T^{1/(2-\gamma)}$ . The widely used relationship  $\Sigma \propto R^{-1} \exp(-R/R_2)$  (e.g. Hartmann 1998; Andrews et al. 2009) is the special case with  $\gamma = 1$ . Considering that  $\nu = \alpha c_s^2/\Omega$ ,  $\gamma = 1$  corresponds to a constant  $\alpha$  value in a disc having  $T \propto R^{-1/2}$  (close to the temperature of a passively irradiated disc).

## 2.2 R - z 2D meridional circulation

Although the disc's 1D evolution is straightforward, the disc's 2D (R-z) accretion structure is much more complicated. The disc's R-z 2D flow structure needs to be self-consistently solved using the fluid equations in the R-z plane. The disc is unlikely to accrete at the same speed at different heights if the disc's vertical structure is considered. The resulting flow pattern shows the meridional circulation. Assuming that the initial density profile at the disc midplane is

$$\rho_0(R, z = 0) = \rho_0(R_0, z = 0) \left(\frac{R}{R_0}\right)^p, \tag{7}$$

and the temperature varies radially (but constant on cylinders)

$$T(R,z) = T(R_0) \left(\frac{R}{R_0}\right)^q,\tag{8}$$

the hydrostatic equilibrium in the R-z plane requires that (e.g. Nelson, Gressel & Umurhan 2013)

$$\rho_0(R, z) = \rho_0(R, z = 0) \exp\left[\frac{GM}{c_s^2} \left(\frac{1}{\sqrt{R^2 + z^2}} - \frac{1}{R}\right)\right],\tag{9}$$

and

$$\mathbf{v}_{\phi}(R,z) = \mathbf{v}_{K} \left[ (p+q) \left( \frac{c_{s}}{\mathbf{v}_{K}} \right)^{2} + 1 + q - \frac{qR}{\sqrt{R^{2} + z^{2}}} \right]^{1/2}, \quad (10)$$

where  $c_s = \sqrt{p/\rho}$  is the isothermal sound speed,  $v_K = \Omega_K R = \sqrt{GM_*/R}$ , and  $H = c_s/\Omega_K$ .

The disc's radial velocity under the cylindrical coordinate system can be derived using the angular momentum equation

$$\frac{\partial \rho \delta \mathbf{v}_{\phi}}{\partial t} = -\frac{1}{R^2} \frac{\partial R^2 T_{R\phi}}{\partial R} - \frac{\rho \mathbf{v}_R}{R} \frac{\partial R^2 \Omega_K}{\partial R} - \frac{\partial T_{\phi z}}{\partial z} - \rho \mathbf{v}_z \frac{\partial R \Omega_K}{\partial z}, \tag{11}$$

where  $\delta v_{\phi} = v_{\phi} - R\Omega_K$ , and T can represent the turbulent Reynolds stress, Maxwell stress, or/and viscous stress. This equation applies to not only axisymmetric flows but also non-axisymmetric flows simply by replacing every term with the azimuthally averaged quantities.

For steady flows (constant  $\rho \delta v_{\phi}$ ) or axisymmetric flows ( $\delta v_{\phi} = 0$ ), we can derive

$$\frac{\rho v_R}{R} \frac{\partial R^2 \Omega_K}{\partial R} = -\frac{1}{R^2} \frac{\partial R^2 T_{R\phi}}{\partial R} - \frac{\partial T_{\phi z}}{\partial z}$$
(12)

after neglecting higher order terms ( $(H/R)^2$  and above). For viscous fluid having  $T_{R\phi} = \mu_{R\phi}R\partial\Omega/\partial R$  and  $T_{\phi z} = \mu_{\phi z}\partial v_{\phi}/\partial z$ , if the viscosity is isotropic with  $\mu_{R\phi} = \mu_{\phi z} = \mu$ , we have

$$\frac{\rho \mathbf{v}_R}{R} \frac{\partial R^2 \Omega_K}{\partial R} = -\frac{1}{R^2} \frac{\partial \left( R^3 \mu \frac{\partial \Omega}{\partial R} \right)}{\partial R} - \frac{\partial \left( \mu \frac{\partial \mathbf{v}_\phi}{\partial z} \right)}{\partial z}. \tag{13}$$

If we assume  $\mu = \rho \nu$ ,  $\nu = \alpha c_s^2 / \Omega$ , and  $\alpha = \alpha_0 (R/R_0)^s$ , and then plug in the density and velocity profiles, we can derive

$$v_R = -\frac{v}{R} \left[ 3s + 3p + 2q + 6 + \frac{5q + 9}{2} \left( \frac{z}{H} \right)^2 \right]$$
 (14)

as in Urpin (1984), Kley & Lin (1992), Rozyczka et al. (1994), Takeuchi & Lin (2002). Thus, if 3s + 3p + 2q + 6 < 0, the flow is outwards at the disc mid-plane. For a commonly adopted disc structure with s = 0, p = -2.25, and q = -0.5, the quantity 3s + 3p + 2q + 6 = -1.75 so that the flow is outwards at the mid-plane. Since 5q + 9 is larger than 0 in this case, the flow can be inwards at the disc surface when z/H is large enough.

On the other hand, turbulence in protoplanetary discs may be highly anisotropic. For example, local MHD shearing box simulations suggest that turbulence induced by the magnetorotational instability (MRI) generates much stronger  $R-\phi$  stress than the  $\phi-z$  stress (Hawley, Gammie & Balbus 1995). However, hydrodynamical simulations suggest that the  $\phi-z$  stress is much stronger than the  $R-\phi$  stress for the vertical shear instability (VSI) (Nelson et al. 2013; Stoll, Kley & Picogna 2017; Flock et al. 2020).

If we can ignore the  $\phi-z$  stress (e.g. for MRI generated turbulence), we can derive

$$v_R = -\frac{v}{R} \left[ 3s + 3p + 3q + 6 + \frac{3q + 9}{2} \left( \frac{z}{H} \right)^2 \right]$$
 (15)

as in Fromang, Lyra & Masset (2011), Jacquet (2013), Philippov & Rafikov (2017). For cases with  $\mu_{\phi z}$  significantly larger than  $\mu_{R\phi}$  (e.g. VSI), we can assume  $\mu_{\phi z} = C\mu_{R\phi}$  (which is equivalent to  $\nu_{\phi z} = C\nu_{R\phi}$  or  $\alpha_{\phi z} = C\alpha_{R\phi}$ ) and we can derive

$$\mathbf{v}_{R} = -\frac{v_{R\phi}}{R} \left[ 3s + 3p + 3q + 6 + \frac{3q + 9}{2} \left( \frac{z}{H} \right)^{2} - Cq \left( 1 - \left( \frac{z}{H} \right)^{2} \right) \right], \tag{16}$$

where  $v_{R\phi} = \mu_{R\phi}/\rho$  is the viscosity generated from the  $R-\phi$  stress. At the disc mid-plane, this equation recovers equation (12) in Stoll et al. (2017). When 3s + 3p + 3q + 6 - Cq < 0, the flow is inwards at the mid-plane. With q = -0.5 and C = 650 (Stoll et al. 2017) for VSI due to the significant motion in the vertical direction (Lin & Youdin 2015), the disc flows inwards at the mid-plane and outwards at  $z \gtrsim H$ .

However, all above derivations are based on the R-z cylindrical coordinate system. Some instabilities (e.g. VSI) show clear distinction between  $R-\phi$  and  $\phi-z$  stresses, so that a cylindrical coordinate system is more appropriate to study disc accretion in these discs (Stoll et al. 2017). On the other hand, some other discs (e.g. MHD discs) have accretion flow which is in a direction more aligned with the radial direction in the spherical polar coordinate system (e.g. Zhu & Stone 2018), and the  $r-\phi$  stress and  $\theta-\phi$  stress play more distinct roles on disc accretion. This motivates us to derive the meridional circulation under the spherical polar coordinate system, which also makes it easier to compare with our spherical polar numerical simulations in Section 3. The angular momentum equation under the spherical polar coordinate system is

$$\frac{\partial \rho \delta \mathbf{v}_{\phi}}{\partial t} = -\frac{1}{r^{3}} \frac{\partial r^{3} T_{r\phi}}{\partial r} - \frac{\rho \mathbf{v}_{r}}{r} \frac{\partial r^{2} \Omega_{K}}{\partial r} - \frac{1}{r \sin^{2} \theta} \frac{\partial \sin^{2} \theta T_{\theta \phi}}{\partial \theta} - \frac{\rho \mathbf{v}_{\theta}}{r \sin \theta} \frac{\partial \sin \theta r \Omega_{K}}{\partial \theta}, \tag{17}$$

where  $v_K = r\Omega_K$ . Throughout the paper, to distinguish the radial direction between the cylindrical and spherical polar coordinate systems, we use R to represent the radial direction in the cylindrical coordinate system, and r for the radial direction in the spherical polar coordinate system. For steady flows with second and higher order terms removed, we have

$$\frac{\rho \mathbf{v}_r}{r} \frac{\partial r^2 \Omega_K}{\partial r} = -\frac{1}{r^3} \frac{\partial r^3 T_{r\phi}}{\partial r} - \frac{1}{r \sin^2 \theta} \frac{\partial \sin^2 \theta T_{\theta\phi}}{\partial \theta}.$$
 (18)

Although solving the same fluid equations under different coordinate systems won't change the results,  $T_{\theta\phi}$  and  $T_{\phi z}$  are very different at the disc surface due to the different curvatures of these two systems, and ignoring  $T_{\theta\phi}$  will lead to a different flow structure than equation (15) which ignores  $T_{\phi z}$ . If we ignore the  $\theta$ - $\phi$  stress and use  $T_{r\phi} = \mu r \partial \Omega_K/\partial r$ , the disc's radial velocity is

$$\frac{\rho \mathbf{v}_r}{r} \frac{\partial r^2 \Omega_K}{\partial r} = -\frac{1}{r^3} \frac{\partial \left( r^4 \mu \frac{\partial \Omega_K}{\partial r} \right)}{\partial r}.$$
 (19)

Assuming  $\mu = \rho \nu$  and  $\alpha = \alpha_0 (r/r_0)^s$  in the spherical polar coordinate system, we can derive

$$v_r = -\frac{v}{r} \left[ 3s + 3p + 3q + 9 + \frac{3q+3}{2} \left( \frac{z}{H} \right)^2 \right].$$
 (20)

By comparing equation (15) with equation (20), we can see that ignoring  $T_{\theta\phi}$  or  $T_{\phi z}$  leads to different flow structures. It is important to choose the appropriate coordinate system so that the different components of the stress from turbulence can be more clearly

separated (e.g. some instabilities may generate turbulence with  $T_{\theta\phi}=0$  but non-zero  $T_{\phi z}$ .).

One particular stress profile that is motivated by MHD simulations is that the stress is vertically uniform until a certain number of disc scale heights ( $z = h_{cut}H$ ) (Fromang et al. 2011). Thus, we write  $\mu$  in equation (19) as

$$\mu = \begin{cases} \alpha \rho_0 \frac{c_s^2}{\Omega_K} \frac{\sqrt{2\pi}}{2h_{\text{cut}}} & |z| \le h_{\text{cut}} H\\ 0 & |z| > h_{\text{cut}} H \end{cases}$$
(21)

so that the vertically integrated stress is still  $\int \mu dz = \alpha \sum c_s^2 / \Omega$ . If  $\mu$  can be written as  $\mu_0 (r/r_0)^\eta$  within  $h_{\rm cut} H$ , the radial velocity within  $h_{\rm cut} H$  is

$$\mathbf{v}_r = -(4.5 + 3\eta)\mu_0 \left(\frac{r}{r_0}\right)^{\eta} \frac{1}{r\rho},\tag{22}$$

where  $\eta = s + p + q + 1.5$ . Comparing equation (22) with equation (20), we can see that the uniform stress case has a sharp increase of velocity at the disc surface (exponential increase due to the  $1/\rho$  dependence).

Different assumptions on the vertical stress profiles due to different accretion mechanisms lead to dramatically different meridional flow structures. The analytical solutions for the meridional circulation (equations 14, 15, 16, 20, 22) will be compared with our direct numerical simulations in Section 3 to mutually verify the analytical derivation and numerical simulations.

## 3 METHODS

We solve the compressible Navier–Stokes equations using the grid-based magnetohydrodynamics (MHD) code ATHENA++ (Stone et al. 2020). We adopt the spherical polar coordinate system  $(r, \theta, \phi)$  for the simulations.

# 3.1 2D disc simulations without planets

We first carry out  $r - \theta$  2D simulations without planets to verify our code by comparing the simulation results with equations (14), (20), and (22). We set up the disc in the domain of r = [0.3, 3.0], and  $\theta =$  $[\pi/2 - 0.5, \pi/2 + 0.5]$ . In the r direction, we have 112 grid cells that are logarithmically uniformly spaced. In the  $\theta$  direction, we have 48 uniformly spaced cells. The disc setup follows equations (7) to (10) with H/R = 0.1 at R = 1, p = -2.25, and q = -0.5. We have adopted the reflecting boundary condition in the  $\theta$  direction and fixed the inner boundary to the initial condition throughout the simulation. The disc relaxes to the initial temperature at a cooling time of  $t_c = 0.01$  orbital time  $(2\pi/\Omega)$ ; Zhu et al. 2015). Such cooling time corresponds to the radiative cooling time-scale at 100 au and is not short enough to trigger VSI (Lin & Youdin 2015). The  $\alpha$  parameter is 0.01. We have carried out three separate simulations with the full viscous stress (equation 13), only the  $r - \phi$  stress, and the vertically uniform stress (equation 21 with  $h_{\text{cut}} = 4$ ). The radial velocities at r = 1 and  $t = 30 T_0$ are shown in Fig. 1, where  $T_0 = 2\pi/\Omega_0$  is the orbital time at r = 1. At 30 orbits, the meridional circulation has been fully established. The three dotted curves which have negative  $v_r$  at the surface in Fig. 1 are the analytical solutions from equations (14), (20), (22) with the same parameters. We can see good agreements between the simulations and the analytical solutions. For comparison, the dotted curve with the positive  $v_r$  at the surface is from equation (16) with  $\alpha_0 = 10^{-4}$ 

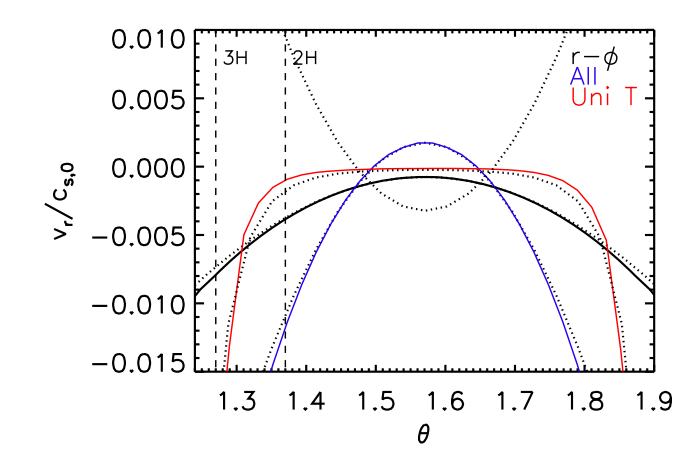


Figure 1. Comparison of the disc radial velocity profiles at r=1 in direct numerical simulations with  $\alpha=0.01$  (solid curves) to the analytic equations (dotted curves). The disc achieves this profile at a time of 30 orbits at r=1. The three dotted curves which have negative  $\mathbf{v}_r$  at the disc surface are analytical solution from equations (14), (20), and (22) with  $\alpha_0=0.01$ . The dotted curve with the positive  $\mathbf{v}_r$  at the surface is from equation (16) with  $\alpha_0=10^{-4}$  and C=650 representing the stress derived in the vertical shear instability simulations. The velocity structure is significantly affected by different vertical stress profiles, although all the  $\alpha_0=0.01$  cases have the same vertically integrated  $r-\phi$  stress.

and C = 650 representing the stress similar to those derived from the vertical shear instability simulations (Stoll et al. 2017).

After testing our code against analytical solutions, we carry out a set of simulations to study the disc surface density evolution for discs having these different vertical stress profiles. These simulations have similar setups as the previous tests except for a few modifications. To study the disc's viscous spread, We setup a Gaussian bump at r=1 with a Gaussian width of 0.1. We also allow  $\alpha$  to change with radii ( $\gamma \neq 1$  in equation 2). We have 680 logarithmically uniformly spaced grids in the radial direction for the domain r=[0.1, 20]. We have 128 uniformly spaced grid cells in the  $\theta$  direction in the domain  $\theta = [\pi/2 - 0.5, \pi/2 + 0.5]$ . The outflow boundary condition and reflecting boundary condition are adopted in the radial and  $\theta$  direction. Our outflow boundary condition, which does not allow the gas to flow from the ghost zones into the computational domain, is different from the default outflow boundary condition in ATHENA++. The simulations are run for 200  $T_0$ .

## 3.2 3D planet-disk interaction simulations

After studying the disc surface density evolution under different stress profiles, we carry out 3D viscous simulations to study the disc's velocity structure influenced by a young planet. The simulation domain covers a range of r = [0.3, 3.0],  $\theta = [\pi/2 - 0.5, \pi/2 + 0.5]$ , and  $\phi = [0, 2\pi]$ . The domain is divided into 112 logarithmically spaced cells in r, 48 uniformly spaced cells in  $\theta$ , and 152 uniformly spaced cells in  $\phi$ . The number of cells in the  $\phi$  direction is half the number required to ensure square cells in the  $r - \phi$  plane; many quantities examined in this paper are azimuthally averaged, therefore this reduction in cells is expected to have a small effect.

To initialize the density profile of the disc, we numerically integrate the density at each grid cell to establish vertical hydrostatic equilibrium. We initialize the sound speed profile using the power-law profile

$$c_{\rm s} = c_{\rm s,0} \left(\frac{r}{r_0}\right)^{-q}.\tag{23}$$

 $<sup>^{1}</sup>z$  and R in these equations are calculated using r and  $\theta$  of each cell in simulations.

As with the 2D simulations, we use power-law exponents of p=-2.25 and q=-0.5 for the density and sound speed profiles, respectively. This gives the disc a surface density profile of  $\Sigma \propto r^{-1}$ , consistent with observations of older protoplanetary discs (Andrews et al. 2009). The disc again has a cooling time of  $t_{\rm c}=0.01$  orbital time and H/R=0.1 at  $r_0$ . We use reflecting boundary conditions in the  $\theta$  direction and fix the radial boundary conditions to their initial values throughout the simulation.

The disc velocity is initialized with only the rotational component  $v_{\phi}$ . To initialize the radial velocity profile, we allow the disc to evolve for a period of roughly 25  $T_0$  and allow the gas to settle into a steady state. With no initial velocity in the  $r-\theta$  plane, the radial velocity of the disc will settle towards equation (14). Once the radial velocity of the disc is properly established, we add a planet at a distance of  $r=r_p=1$  from the central star. The planet increases in mass over the next 25 orbits from zero up to its final mass  $M_p$ . The gravitational potential of the planet is written as a second-order potential (e.g. Dong et al. 2011):

$$\Phi_{\rm p} = -GM_{\rm p} \frac{1}{\left(r^2 + r_{\rm s}^2\right)^{1/2}},\tag{24}$$

where  $r_s$  is the smoothing radius. We choose the value of  $r_s$  to be 0.1 Hill radii for each simulation. After reaching its final mass, the planet continues to open a gap in the disc for another 450 planetary orbits, giving the simulation a total time of 500  $T_0$ .

The 3D simulations have the isotropic disc viscosity  $\alpha$  and the final planet mass  $M_p$  as free parameters. We choose final planet masses of  $10^{-3}$  and  $10^{-2}$  central star mass (which are  $1\,M_J$  and  $10\,M_J$  if the central star is a solar mass star) in combination with a constant  $\alpha$  of  $10^{-3}$  and  $10^{-2}$ , creating a set of four different simulations. We also run a second set of simulations to study how the choice of the smoothing length affects the unbound velocity flow in the vicinity of the planet, which we discuss in Section 4.2. These simulations use the same disc viscosities of  $\alpha = 10^{-3}$  and  $10^{-2}$ , final planet masses of  $1\,M_J$  and  $10\,M_J$ , but a constant smoothing length of 2 grid cells. In order to examine the effect of MHD discs on meridian circulation, we run an additional simulation with a final planet mass of  $1\,M_J$  and a vertically varying  $\alpha$  according to equation (21), with  $h_{\rm cut} = 4$ .

#### 4 RESULTS

## 4.1 Disc density evolution with different stress profiles

Fig. 1 shows that the disc's velocity structure is significantly affected by different vertical stress profiles in discs without planets. At two disc scale heights ( $\theta \sim 1.37$ ), the full stress case has an inward velocity  $\gtrsim 0.01c_s$ , the  $r-\phi$  stress only case has an inward velocity of  $\sim 0.004c_s$ , the uniform stress case has an inward radial velocity  $\leq 0.001c_s$ , and the VSI case has an outward velocity  $\geq 0.01c_s$ . However, at three disc scale heights, the inward radial velocity in the uniform stress case quickly increases to  $\gtrsim 0.015c_s$ . Note that all three cases with  $\alpha = 0.01$  in Fig. 1 have the same vertically integrated  $r - \phi$  stress, which means that they have the same  $\alpha$  value in the traditional 1D viscous disc theory. If we also set  $\alpha = 0.01$  in the VSI stress profile, the velocity profile will be amplified by 100 and out of the plotted range. Considering that strong molecular lines (e.g. CO) mostly trace the disc atmosphere, the probed velocity will be very sensitive to different vertical stress profiles in the disc, even if different stress profiles correspond to the same  $\alpha$  value in 1D disc evolution. We caution that this traditional viscous stress model has limitations to capture internal stresses due to large-scale magnetic fields (e.g. Zhu & Stone 2018) or external

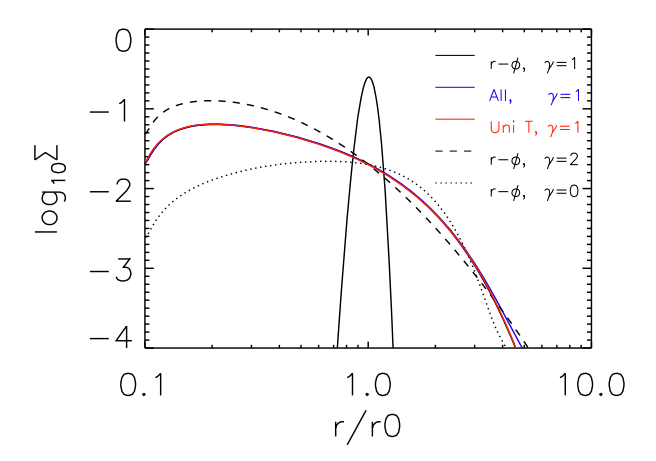


**Figure 2.** Viscous disc evolution for discs with different stress structures. The Gaussian profile at  $r = r_0$  is the initial condition. All other curves are the disc surface density at  $200 T_0$  where  $T_0$  is the orbital time at  $r = r_0$ .

stresses due to magnetocentrifugal wind (Bai 2016). Nevertheless, future kinematic observations using various molecular lines tracing different disc heights will not only measure the value of  $\alpha$  but also constrain the detailed vertical stress profiles and accretion mechanisms.

These largely different velocity structures with different vertical stress profiles raise the question as to whether the surface density evolution of 3D viscous discs are also affected by the detailed vertical stress profiles, so that the traditional 1D disc evolutionary model (equation 3) cannot capture the disc evolution properly. Thus, we have carried out axisymmetric 2D simulations with different stress profiles in the disc to study the spread of a Gaussian bump. The results are shown in Fig. 2. With the same vertically integrated stress, all three simulations with three different vertical stress profiles (black, blue, and red solid curves) show exactly the same surface density structure at  $200\,T_0$ , following a power law  $R^{-1}$  before the exponential decrease (equation 6). This demonstrates that the detailed vertical stress profiles do not affect the disc surface density evolution, and the traditional 1D viscous model is sufficient for studying the disc surface density evolution.

As shown in Fig. 2, we have also carried out full stress simulations whose vertically integrated stress varies along the radial direction steeper or flatter than  $\nu \propto R$ . If the vertically integrated stress changes slower with radii (e.g.  $\gamma=0$  in equation (2) which means  $\alpha \propto R^{-1}$  with  $T \propto R^{-1/2}$ ), the surface density follows a flatter power law before a steeper exponential decrease, as predicted by 1D model in equation (6).

Recent kinematic measurements from Dullemond et al. (2020) have suggested that, at the disc outer edge of HD 163296, the disc surface density falls faster than  $\exp(-R/R_{\rm d})$  and is closer to  $\exp(-(R/R_{\rm d})^2)$ . Although Dullemond et al. (2020) suggests that this sharper density drop is due to outside-in photoevaporation or truncation by an unseen companion, we suggest that it can also be due to the viscosity's power law having  $\gamma < 1$  or  $\alpha$  decreases with larger radii. For example, when  $\gamma = 0$  or  $\alpha \propto R^{-1}$  with  $T \propto R^{-1/2}$ , equation (6) becomes  $\Sigma \propto R^0 \exp(-(R/R_2)^2)$  (the dotted curve in Fig. 2). This sharper drop is then consistent with observations in Dullemond et al. (2020). Another implication of the decreasing  $\alpha$  with the increasing radius is that the density profile at the inner disc would be a constant with radii ( $\propto R^0$ ). Some discs indeed show a relatively flat surface density profile (e.g. Carrasco-González et al. 2019). On the other hand, measurements of the disc surface density at the inner disc

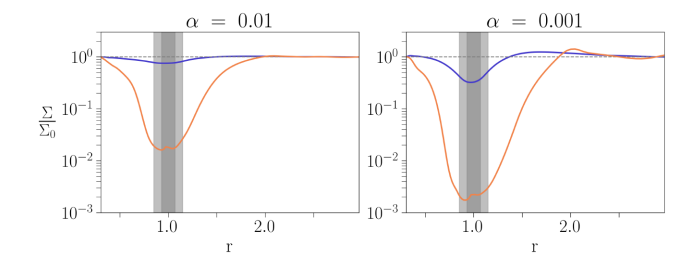


**Figure 3.** Radial surface density profiles for the  $\alpha = 0.01$  simulations (left-hand side) and  $\alpha = 0.001$  simulations (right-hand side) at  $t = 500 T_0$ . Blue curves indicate a planet of 1 Jupiter mass, and orange curves indicate a planet of 10 Jupiter masses.

could be very uncertain due to the optical depth effects (Carrasco-González et al. 2019; Liu 2019; Zhu et al. 2019)

#### 4.2 Non-axisymmetric velocity structure induced by the planet

After presenting the results on the disc structure without planets, we will study how the planet can influence the disc structure.

Fig. 3 shows the disc surface density profiles at  $t = 500 T_0$  when the gap is fully opened by the planet. Blue curves represent  $1M_J$  simulations while orange curves represent  $10M_J$  simulations. The grey shaded regions denote the width of the planet's Hill sphere for 1 and 10 Jupiter masses. Larger gaps are formed in the presence of higher mass planets or lower viscosity discs (e.g. Fung, Shi & Chiang 2014; Kanagawa et al. 2015).

Figs 4 and 5 show the velocity components of the disc for the  $\alpha=0.01, 1M_J$  and  $\alpha=0.01, 10M_J$  simulations, respectively. Each row shows the disc velocities for a different scale height, with panels showing the vertical velocity  $v_z$ , the radial velocity  $v_r$ , and the deviation from Keplerian velocity  $\delta v_\phi$ . The density panel (at top left) shows the gap and spiral wake. The streamline of a horseshoe trajectory (starting at the red point) outlines the gap region. To examine the velocity components across different disc scale heights, we cut the disc at equally spaced values of constant  $\theta$ . All of our poloidal cuts are taken on the upper half of the disc; any cuts on the lower half would be almost identical, save for a change in the sign of  $v_z$  or  $v_\theta$ . We note that this is a simple way to analyse quantities at different disc scale heights and may not reflect the velocity structure at constant h/r throughout the disc.

The vertical velocity v<sub>7</sub> (left-hand column) shows the presence of inflows in the vicinity of the planet (Morbidelli et al. 2014; Fung, Artymowicz & Wu 2015). The radial velocity (middle column) clearly follows the spirals. For both the inner and outer spirals at the mid-plane, the disc region outside the spiral has negative  $v_r$  while the region at r smaller than the spiral front has positive  $v_r$ . The gap is not apparent in the  $v_r$  panels. On the other hand, regions of sub/super-Keplerian velocity, shown as  $\delta v_{\phi}$  (right-hand column), trace the edges of the gap very well. The disc is super-Keplerian (positive  $\delta v_{\phi}$ ) at the outer gap edge, while it is sub-Keplerian (negative  $\delta v_{\phi}$ ) at the inner gap edge. This is much clearer in Fig. 5, as the velocities in the  $1M_J$ simulation are dominated by the overall sub-Keplerian rotation of the gas. Meanwhile, the spirals are not as visible in the  $\delta v_{\phi}$  panel. Overall, we conclude that  $v_r$  traces the spirals while  $\delta v_{\phi}$  traces the gap.  $v_z$  has a smaller amplitude than either  $v_r$  or  $\delta v_{\phi}$ . Since our temperature profile is nearly isothermal, we do not observe additional spirals driven by vertical buoyancy resonances (Bae et al. 2021). However, when present these spirals will appear in the disk velocities as additional sprial signatures traced by the  $v_r$  and  $v_z$  components.

We also observe some height dependence for all three velocity components, especially for the  $10M_J$  case which has a deep gap. Around the planet,  $v_z$  is more negative at 1 scale height than 2 scale heights, implying a higher inflow velocity closer to the planet, while the amplitude of  $\delta v_\phi$  is higher at the mid-plane decreasing towards the surface. In the  $10M_J$  case,  $v_r$  changes quite dramatically at different disc heights. The large  $v_r$  around the planet which traces the spirals at the mid-plane disappears at 1 scale height and only slightly comes back at 2 scale heights, and the  $v_r$  tracing the spirals at the very inner disc becomes stronger at 2 scale heights. Thus, for massive planets in a deep gap, the kinematic signatures of the planet may show some differences by using various molecular tracers probing different depths in the disc.

The region around the planet is significantly affected by the planet in both  $v_r$  and  $\delta v_\phi$  panels, which can be probed by the distortion in the velocity channel maps (Pinte et al. 2018). The circumplanetary region can be divided into two regions: the region that is bound to the planet (e.g. the circumplanetary disc) and the unbound region which is circulating between the planet and the star (Lubow, Seibert & Artymowicz 1999). The bound circumplanetary disc has a circular motion around the planet, and for our simulations it is not completely resolved since the circumplanetary disc is quite small ( $\lesssim 0.4\,R_H$  where  $R_H = (M_p/3M_*)^{1/3}a$ ; Martin & Lubow 2011). Thus, we will only focus on the unbound region for studying the velocity distortion.

The large velocity in the unbound region is associated with the spirals which are strongest close to the planet. We calculate the deviation from Keplerian velocity as  $\delta v_K = \sqrt{v_r^2 + \delta v_\phi^2}$  around the planet. In Fig. 7, we plot  $v_{max} = max(\delta v_K)$  for each simulation against the final planet mass  $M_p$  for several different scale heights in the disc. This maximum velocity deviation should be close to the maximum 'kink' velocity measured in observations (e.g. fig. 1 of Pinte et al. 2018). For this figure, we plot the  $1M_J$  and  $3M_J$ simulations with a smoothing length of 2 grid cells, as well as the  $10M_I$  simulations with the smoothing length scaled to the planet mass. To ensure we do not measure the circumplanetary disc, we ignore values within the planet's Hill sphere while calculating v<sub>max</sub>. We tried excluding different sized regions (e.g.  $0.4 R_H$ ) or using simulations with different smoothing lengths, and found the results to be almost identical. Above three scale heights, v<sub>max</sub> increases dramatically and no longer follows the relationship found at lower scale heights. We believe that these large velocities are numerical in nature, created by the gas density dropping to the simulation density floor in the disc atmosphere. Thus, we did not plot the values beyond three scale heights in Fig. 7. For the case with the  $10 M_J$  planet in an  $\alpha = 0.001$  disc, we did not plot  $v_{max}$  at 2 scale heights and above where the density reaches the floor inside the deep gap.

Fig. 7 shows that, for 1 and  $3\,M_J$  cases,  $v_{max}$  does not depend on  $\alpha$  or the disc height where it is measured. But for  $10\,M_J$  cases,  $v_{max}$  decreases from the mid-plane to two scale heights and then increases beyond two scale heights. This is also apparent from Fig. 5 where  $v_r$  becomes small at 1 and 2 scale heights.

Our best fit for the values taken at the disk mid-plane is plotted as the grey line, which is

$$v_{max} = 54v_K \frac{M_p}{M_*},\tag{25}$$

where  $v_K$  is the planet's Keplerian velocity around the star. If we apply equation (25) to the observation in Pinte et al. (2018), the 0.15  $v_K$  deviation in their Fig. 1 corresponds to a 5.4  $M_J$  planet around a 1.9  $M_{\odot}$  star. This is higher than the 2  $M_J$  planet that Pinte et al. (2018) derived by comparing channel maps between observations

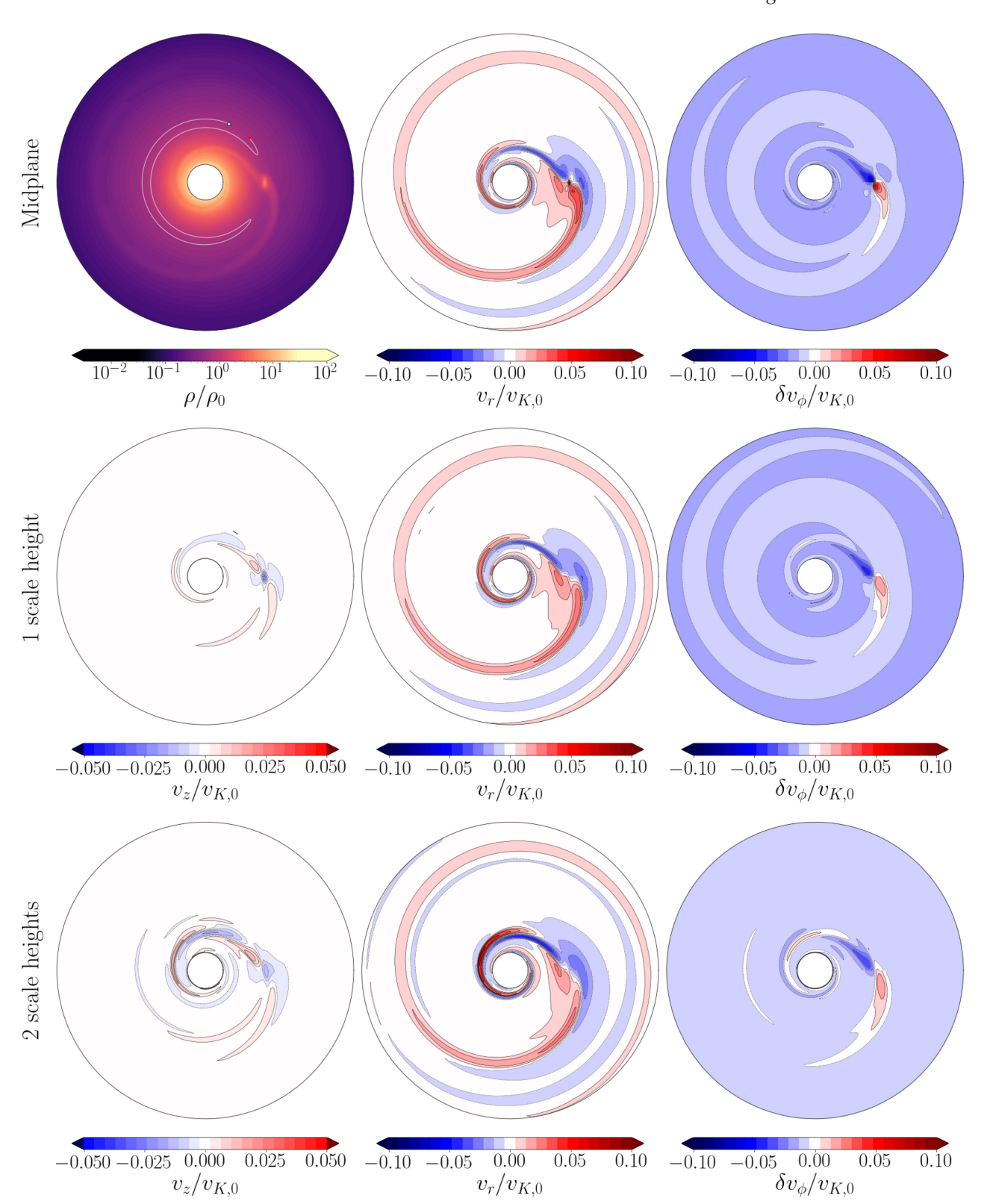
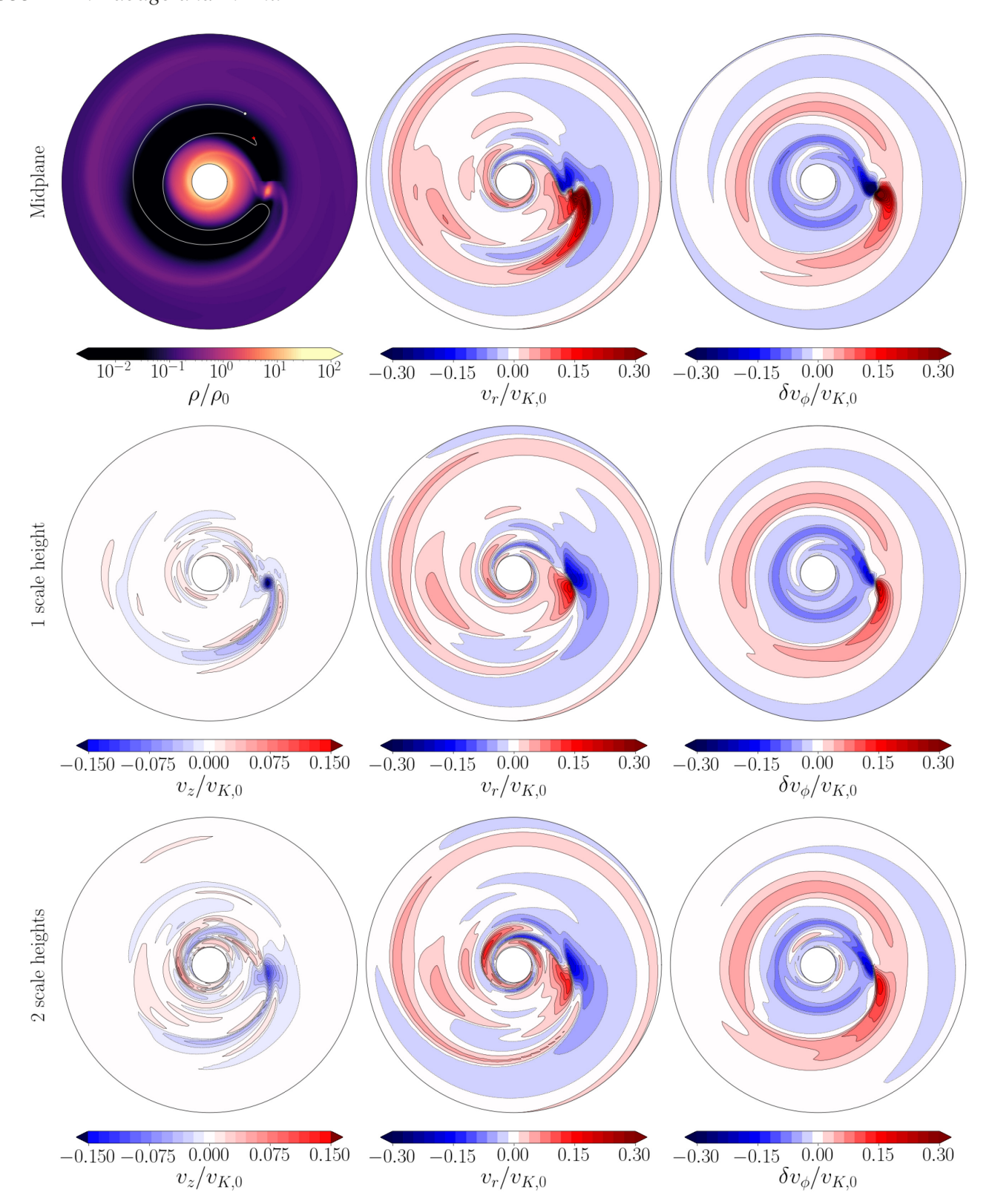


Figure 4. Mid-plane cuts of the  $\alpha=0.01, M=1M_J$  simulation at  $t=500\,T_0$ . Each row shows the velocity components of the disc at different disc heights (mid-plane, 1 scale height, and 2 scale heights). Top left-hand column: Density plot, with a horseshoe trajectory also plotted within the gap region, beginning at the red marker. Left-hand column: vertical velocity  $v_z$ . Middle column: Radial velocity. The inward/outward radial velocity trace the inner/outer spirals. Right-hand column: Deviation from Keplerian velocity. Regions of sub-Keplerian and super-Keplerian velocity trace the inner and outer gap edges. All velocities are scaled to the local Keplerian velocity at R=1.



**Figure 5.** Same as Fig. 4, but for the  $\alpha = 0.01, M = 10M_J$  simulation.

and direct simulations. Although this difference may be attributed to that we did not carry out synthetic channel maps, we notice that our  $\delta v_K$  around the planet  $(M_p/M_* = 0.001 \text{ cases})$  is indeed lower than that shown in Pinte et al. (2018) (their fig. 4) by a factor of 2. On the other hand, our values seem to be more consistent with Pérez

et al. (2018) (their Fig. 1). Thus, more detailed comparisons among these simulations with the same parameters are needed in future. We note that at the disc mid-plane, our fit in Fig. 7 has little dependence on the choice of  $\alpha$ . Even if  $\alpha$  changes by one order of magnitude ( $\alpha = 10^{-3}$  and  $10^{-2}$ ), the maximum velocities of  $\delta v_K$  for both 1  $M_J$ 

and  $10~M_J$  cases are almost identical. Thus, we can safely use this relationship to derive the embedded planet mass, with a minimum impact from the unknown disc viscosity. From this perspective, using the 'kink velocity' serves as a more robust method to derive the planet mass than using properties of the gap (e.g. Zhang et al. 2018) which depends on both  $\alpha$  and the gas scale height.

The independence of  $v_{max}$  on  $\alpha$  indicates that the maximum velocity of  $\delta v_K$  is not related to the disc's accretion process. Instead, it is more likely determined by the planet–disc gravitational interaction. The linear dependence between  $v_{max}$  and  $M_p$  seems to be consistent with the linear theory (Goldreich & Tremaine 1979) which shows that, for small amplitude perturbations, the velocity perturbation is proportional to the planet mass. However, the spirals can quickly become highly non-linear when the planet mass is large (Goodman & Rafikov 2001; Muto, Suzuki & Inutsuka 2010; Dong et al. 2011; Zhu, Stone & Rafikov 2013). The spirals steepen to shocks when they propagate away from the planet at a distance of

$$|\Delta r_{\rm sh}| \approx 0.93 \left(\frac{\gamma + 1}{12/5} \frac{GM_{\rm p}\Omega_{\rm p}}{c_{\rm s}^3}\right)^{-2/5} H,\tag{26}$$

where  $\gamma$  is the adiabatic index. Thus, the shocking distance is  $\sim H$ and  $\sim 0.4H$  for the  $1 M_J$  and  $10 M_J$  planet in our H/R = 0.1 disc. Since we only measure  $v_{max}$  in the region beyond the planet's Hill radius (which is 0.7H and 1.5H for  $1M_J$  and  $10M_J$  cases), the measured spirals are in the non-linear regime (especially for  $10 M_J$ cases). Furthermore, a deep gap is induced by the massive planet, which clearly indicates that the linear theory cannot be applied to the massive planet case. Thus, we need to sort a different explanation for the measured  $v_{\text{max}}$  with a massive planet. For massive planets (e.g.  $10\,M_J$ ), the flow may be quite dynamic. The circumplanetary region is well separated from the background disc, and we expect that the maximum velocity of disc material in a horseshoe orbit should scale with the free-fall velocity to the circumplanetary disc edge. Since the circumplanetary disc has a size of  $\lesssim 0.4 R_H$ , the unbound flow will have a maximum velocity at the closest approach at  $\sim$ 0.4  $R_H$ , similar to the escape velocity at  $\sim 0.4 R_H$ , which is  $v_{\rm esc} = 2.7 v_K (M_p / M_*)^{1/3}$ . For a  $10 M_J$  planet around a solar mass star,  $v_{\rm esc} = 0.58 v_K$ , which is close to our measurement of  $0.5 v_K$ . On the other hand, the escape velocity scales with  $M_{\rm p}^{1/3}$ , while our fitting shows a linear scaling with  $M_p$ . For a  $M_J$  planet, the escape velocity at  $0.4R_H$  is higher than our measured v<sub>max</sub>. We attribute this to the fact that the gas flow is significantly affected by the gas pressure within the shallow gap induced by a low mass planet and the linear perturbation theory may apply.

# 4.3 Azimuthally averaged velocity structure induced by the planet

Fig. 8 shows the velocity structure of the disc, azimuthally averaged in the  $r-\theta$  plane at  $t=500\,T_0$ . All velocities are scaled relative to the local sound speed. The poloidal velocity is shown as black arrows, while the background colour denotes the gas rotational speed. The blue and red areas denote regions of sub- and super-Keplerian rotation, respectively. Meridional flows are visible in all simulations around the planet's Hill radius (denoted by the orange circle at R=1). The circulation is stronger in discs with a deeper gap. To maintain figure readability, we only display vectors every three grid cells, and exceedingly large velocities (which typically occur towards the disc atmosphere) have been omitted.

Although the meridional flow shown in Fig. 8 is regarded as an evidence of the presence of a planet (Teague et al. 2019), such flow motion is highly non-axisymmetric in nature. As shown

in Fig. 6, although the planet's gravity leads to strong inflow to the planet from the planet's polar direction (Tanigawa, Ohtsuki & Machida 2012; Fung et al. 2015; Szulágyi et al. 2016), such inflow motion is localized around the planet. At  $\phi=\phi_p+\pi$ , there is no such meridional motion present. Thus, understanding whether the observed meridional motion is truly axisymmetric in discs (e.g. similar meridional patterns at different values of  $\phi$ ) or whether it only occurs in some local disc region is important for confirming its planet origin.

A detailed examination of the azimuthally averaged velocity is shown in Fig. 9. We examine each velocity component across the entire (cylindrical) radial extent and vertical extent of the disc, using the same polar cuts used in Figs 4 and 5 to examine different scale heights. The disc scale heights are visible in Fig. 8 as grey dashed lines in the upper half of the disc. We plot the azimuthally averaged velocities at the end of the simulation ( $t = 500\,T_0$ ), and remove all cells within the Hill sphere of the planet to remove local effects from the planet's vicinity. Since the number of  $\theta$  cells in our simulations is even, the mid-plane velocity is calculated by averaging the two cells just above and below the mid-plane.

The  $\delta v_{\phi}$  panels (top panels) in Fig. 9 show a vertical shift as one moves vertically upward from the disc mid-plane, a feature we attribute to the gas pressure gradient. The displacements are more noticeable in discs with smaller perturbations relative to the disc Keplerian speed (this is also true relative to the local sound speed  $c_s$ , since  $h/r = c_s/v_\phi$  is assumed a constant vertically). The magnitude of the velocity shift induced by the pressure gradient is at most a few percent of the Keplerian velocity. In spite of the vertical shift, the shape of the curve is unchanged below 3 scale heights. By comparing these curves with the surface density plots (redrawn at the top of the figure), we see that the points of minimum and maximum deviation correspond to the points of steepest pressure gradient, and the magnitude of the deviation is roughly equal to the value of the background pressure gradient at the gap edges, similar to that described in Teague et al. (2018). Above 3 scale heights, the residual velocities in the inner disc become highly negative, larger than expected for the given planet and disc parameters.

Zhang et al. (2018) and Gyeol Yun et al. (2019) have studied the deviation from Keplerian velocity produced at the gap edge and how the velocities change with different disc parameters. On the other hand, these works are based on 2D simulations, so that they focus on the velocity deviation at the disc mid-plane, while most ALMA molecular line observations actually probe the disc surface (Teague et al. 2018, 2019). These studies have found relationships between the parameters of the planet–disc system and the amplitude of the velocity deviations  $\Delta(\delta v_{\rm rot})$  (measured from the sub-Keplerian minimum interior to  $R_{\rm p}$  to the super-Keplerian maximum exterior to  $R_{\rm p}$ ). The dependence of the planet–disc parameters are commonly expressed in terms of a fitting parameter K, where  $K=q^{pa}\left(\frac{h}{r}\right)^{pb}\alpha^{pc}$  and the power-law exponents pa,pb, and pc are to be determined.

Gyeol Yun et al. (2019) run a parameter study using the fitting parameter  $K=q^2\left(\frac{h}{r}\right)^{-5}\alpha^{-1}$  from Kanagawa et al. (2015). They find a fit of

$$\Delta(\delta v_{\text{rot}}) = \left(\frac{h}{r}\right) \frac{0.007K^{1.38}}{1 + 0.06K^{1.03}}.$$
 (27)

In a different parameter study by Zhang et al. (2018), both K and  $\Delta(\delta v_{rot})$  are fit to the simulation data, with

$$K_{\rm v_r} = q \left(\frac{h}{r}\right)^{-1.27} \alpha^{-0.41},$$
 (28)

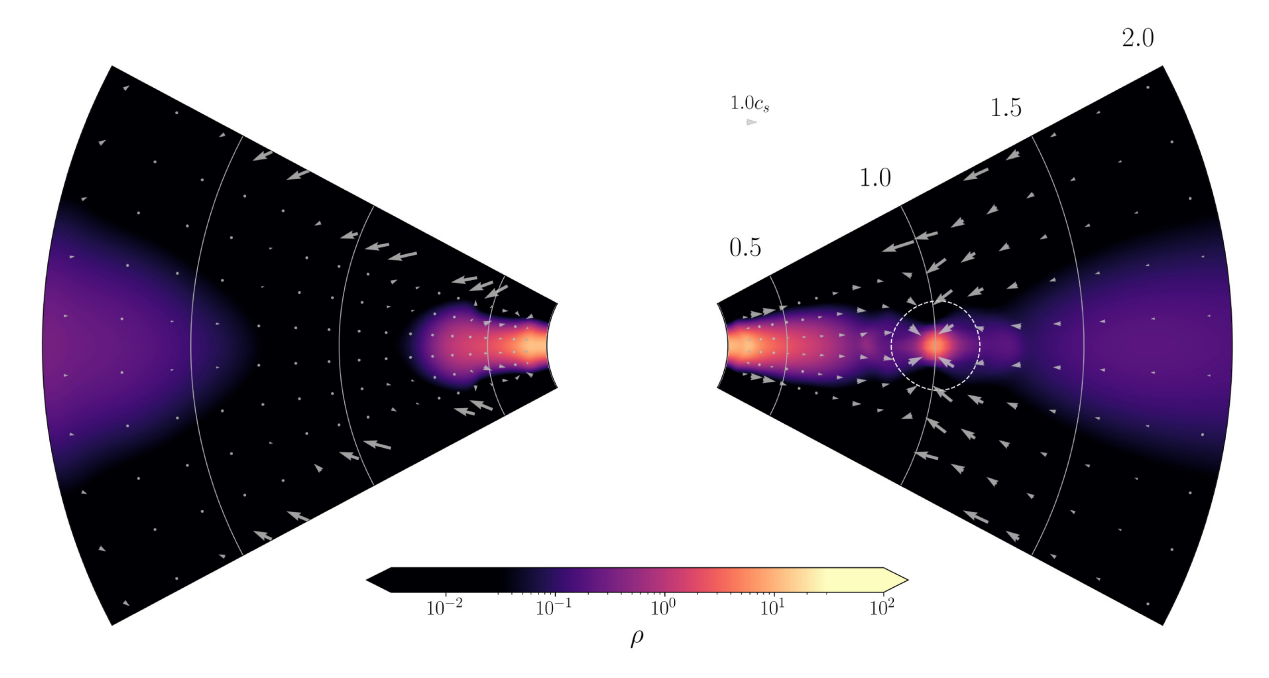


Figure 6. Vertical slice of the  $\alpha = 0.01$ ,  $M = 10M_J$  simulation at  $t = 500 T_0$ . Background contours show gas density. Dashed circle on the right wedge denotes the planet's Hill radius. Vectors denote the gas velocity, scaled to the local sound speed.

and

$$\Delta \left( \delta \mathbf{v}_{\text{rot}} \right) = 0.11 K_{\mathbf{v}_r}^{0.80}. \tag{29}$$

Both of these parameter studies used 2D hydrodynamic simulations, and thus were unable to study how  $\Delta(\delta v_{rot})$  changes at different disc scale heights. In Fig. 10, we plot  $\Delta(\delta v_{rot})$  at different disc heights with respect to K and  $K_{v_r}$  in our simulations, together with the two fitting formulas (equation 27 on the left and equation 29 on the right). We can see that both formulas fit equally well at large K and  $K_{v_r}$  values. But equation (27) fits slightly better than equation (29) for small K and  $K_{v_r}$  (which means smaller mass planets). Most importantly,  $\Delta(\delta v_{rot})$  is almost a constant within 3 disc scale heights. For larger values of K and  $K_{v_r}$  (e.g. discs with larger planets, smaller scale heights, or lower values of  $\alpha$ ), the value of  $\Delta(\delta v_{rot})$  begins to deviate above 3 scale heights. This indicates that the deviation from the Keplerian velocity increases towards the disc surface faster in a deeper gap.

At 4 scale heights, closer to the disc atmosphere, we find that  $\Delta(\delta v_{rot})$  departs strongly from the expected behaviour and increases substantially to roughly order unity. Since  $\delta v_\phi = v_\phi - R\Omega_K = v_\phi - v_K$ , the large values of  $\Delta(\delta v_{rot})$  suggests that  $\delta v_\phi$  is changing by nearly the local Keplerian velocity in the vicinity of the gap. Examining the azimuthal velocities in Fig. 9 shows that the super-Keplerian peak in  $\delta v_\phi$  is  $\lesssim 10$  per cent of Keplerian velocity at 4 scale heights, suggesting that most of the contribution to  $\Delta(\delta v_{rot})$  is from sub-Keplerian motion. Thus, a possible interpretation of this feature is that, in the vicinity of the gap, material in the disc atmosphere has lost nearly all of its rotational velocity and is instead falling directly towards the star.

Overall, as long as the molecular tracers (Isella et al. 2018) are tracing the disc region within  $\sim$ 3 disc scale heights, we can use equations (27) and (29) to derive the planet mass from the change of the azimuthal velocities. If the tracers are tracing the region beyond  $\sim$ 3 disk scale heights, using equations (27) and (29) can overestimate the planet mass. Emission from different molecular tracers is visible at different vertical disc heights due to different

optical depths (Flaherty et al. 2017), so comparing observations from different molecular tracers, such as the different CO isotopologues, may allow observations to distinguish velocities at different disc scale heights.

The disc radial velocities (Fig. 9, middle row) show a similar profile to the azimuthal velocity in the vicinity of the planet. These features are the signature of the 'planet-driven' flows where the planet moves material out of the gap. Interior to  $r_p$ , there is a decrease in the radial velocities (even to negative values), while exterior to  $r_p$  there is an increase. This is most apparent in the  $M_p = 10M_J$  simulations. These flows are strongest at the disc mid-plane and weaken as one moves vertically in the disc; for most of our simulations, these flows are no longer visible above 2 scale heights. Some simulations show a reversed radial flow direction in the disc atmosphere, with  $v_r$  positive interior to  $r_p$  and negative exterior to  $r_p$ . This reversal may correspond to the material at the surface flowing into the gap. The appearance of these local extrema in the radial velocity channel is a signature unique to the planet and may be important in determining the existence of a planet in an observed gap. Section 5 examines this idea further by comparing the velocity fields of planetary and non-planetary gaps.

Gas inflows are also visible in the disc poloidal velocities (Fig. 9, bottom row), as velocity peaks at the planet's orbital radius (except for the velocity at 4 scale heights). Since the data in Fig. 9 are taken from the upper half of the disc, the inflows appear as a positive bump near r=1. The inflow pattern is visible for several scale heights, though the magnitude of these features is not as large as the  $\delta v_{\phi}$  signature. We note that, for the  $10M_J$  simulations, additional downward motion at  $R \sim 1.5$  appear outside of the planet's orbital radius; this is also visible in Fig. 8.

## 5 DISCUSSION

## 5.1 Predicting the 'kink velocity' for the DSHARP sample

The velocity disturbances created by the planet in Figs 4 and 5 trace features that span across the entire disc, some of which are present

**Table 1.** Estimated velocity deviations for selected discs using equation (25), in units of the local Keplerian velocity. Distance and stellar mass data from Andrews et al. (2018) and planet mass estimates from Zhang et al. (2018). Gap distances are measured in AU and used as the planet–star distance. Star masses are given in  $M_{\odot}$ , and planet masses are given in  $M_{\rm J}$ . The 'middle' planet mass estimates are taken from the middle values of Column 13 in Zhang et al. (2018). Values in  $\delta v_{\rm obs}$  are the maximum velocity deviations from Pinte et al. (2020), where applicable.

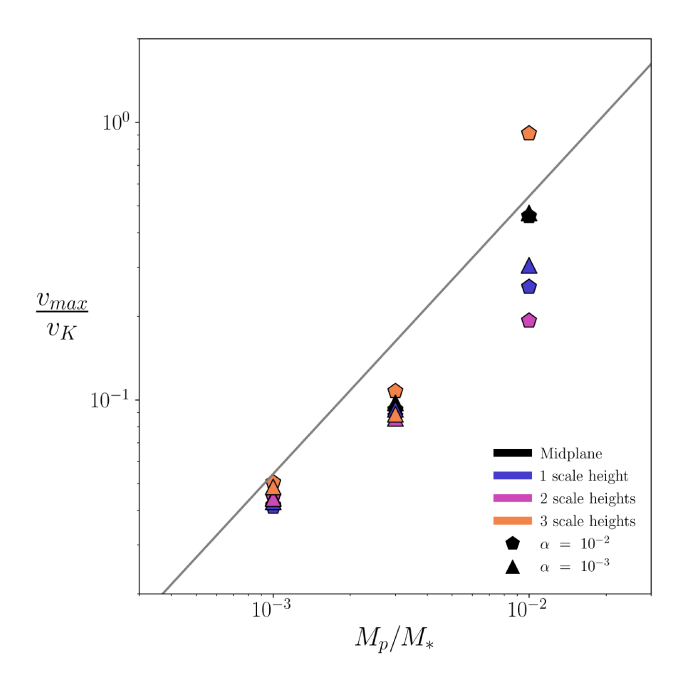
Disc	Gap (AU)	$M_*(M_\odot)$	$M_{\rm p,\;min}$	$M_{\rm p}$	$M_{\rm p,  max}$	$\delta v_{min}$	$\delta { m v}$	$\delta v_{\text{max}}$	$\delta v_{obs}$
AS 209	9	0.83	0.37	3.38	4.18	0.0241	0.22	0.272	_
AS 209	99	0.83	0.18	0.75	1.32	0.0117	0.0488	0.0859	_
Elias 24	57	0.78	0.19	0.81	1.72	0.0132	0.0561	0.119	_
Elias 27	69	0.49	0.02	0.1	0.12	0.0022	0.011	0.0132	?
GW Lup	74	0.46	0.01	0.06	0.06	0.00117	0.00704	0.00704	< 0.3
HD 142666	16	1.58	0.09	0.5	0.62	0.00308	0.0171	0.0212	_
HD 143006	22	1.78	2.35	9.81	40.6	0.0713	0.298	1.23	$\approx 0.20$
HD 143006	51	1.78	0.14	0.57	0.67	0.00425	0.0173	0.0203	_
HD 163296	10	2.04	0.19	1.18	1.46	0.00503	0.0312	0.0386	_
HD 163296	48	2.04	0.54	2.24	4.45	0.0143	0.0593	0.118	_
HD 163296	86	2.04	0.08	0.34	0.34	0.00212	0.009	0.009	$\approx 0.15$
SR 4	11	0.68	0.38	3.57	4.41	0.0302	0.283	0.35	_

across multiple scale heights. These disturbances are strongest in the vicinity of the planet, and so good azimuthal resolution is desirable in observations. For discs with high azimuthal resolution (roughly  $\lesssim 1R_H$ ), deviations from Keplerian velocity can be localized to specific areas in the disc, which has been used to infer the presence and position of planets using velocity channel maps (Pinte et al. 2018, 2020).

Given a mass for the embedded planet, equation (25) can be used to predict the velocity deviation created in the disc. In Table 1, we calculate the expected velocity deviations ('kink velocity') for planets in selected discs. We use planet masses from Zhang et al. (2018). For the 22 AU gap in HD 143006, our calculated value for  $\delta v$  is roughly consistent with the measured value obtained in Pinte et al. (2020). On the other hand, most planet masses constrained by Zhang et al. (2018) for the DSHARP sample are less than  $M_J$ , which corresponds to  $v_{max}/v_K \lesssim 0.05$  (Fig. 7), which requires high spectral resolution observations. For some cases (e.g. the 86 AU planet candidate in HD 163296), our predicted 'kink' velocity is significantly smaller than observations in Pinte et al. (2020), which indicates some inconsistency between the planet mass estimate using the dust continuum method and the mass estimate using the gas kinematic method. To understand this inconsistency, it is crucial to constrain the gaseous gap depth and width, which can also be used to derive the planet mass (e.g. Fig. 10) without assuming some dust size in the disc (as in the dust continuum method).

# 5.2 Azimuthally averaged velocity structure for a gap without a planet

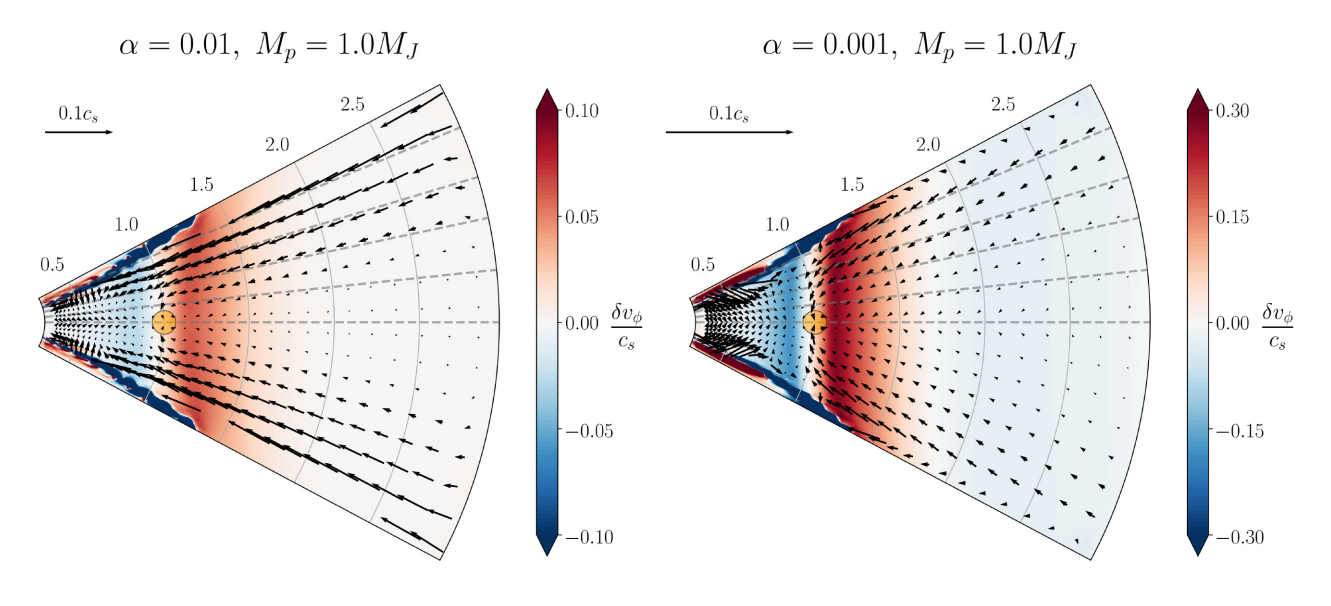
Although Fig. 10 links the planet mass with the gas kinematics at the gap edge, we want to note that the gas kinematics measurements in Teague et al. (2018, 2019) are actually signatures of a local decrease in the gas surface density, and they are not direct probes for the embedded planet. For the gas, there is a radial force due to the pressure gradient  $\frac{dP}{dr}$ , and the change in the pressure gradient due to the gap causes a change in the azimuthal velocity  $v_{\phi}$ . The strength of the meridional flows observed in the disc atmosphere is also a function of gap depth, as the flows angle more strongly in the polar direction over the gap. However, neither of these is a direct signature of an embedded planet; a gap created by non-planetary means with a similar gap depth would exhibit the same deviations in azimuthal velocity and gap inflows, despite no planet existing within the gap.



**Figure 7.** Maximum deviation from Keplerian velocity  $v_{max}$  versus planet mass  $M_p$ , across multiple scale heights of the disc.  $v_{max}$  is scaled to the local Keplerian velocity. Triangle and pentagon markers correspond to disc viscosities of  $\alpha=0.001$  and  $\alpha=0.01$ , respectively. The grey line represents a linear relationship between  $v_{max}$  and  $M_p$ , as described in the text.

Thus, we want to compare the velocity fields in gaps created by planetary and non-planetary methods in order to identify any velocity signatures that are unique to the planet. To do this, we extend our simulations by removing the planetary mass and simulating an additional time of  $50\,T_0$ . Without the gravitational influence of the planet, any unique dynamic planetary signatures are dispersed within several orbits. This roughly mimics the gaps created by non-planetary methods which may operate more axisymmetrically, such as snow lines and MRI, even though no additional physics has been implemented in our model. We note that the gap slowly closes over tens ( $\alpha=0.01$  cases) or hundreds ( $\alpha=0.001$  cases) of orbits due to the viscous spreading.

A snapshot of the original, 'planetary' gap is compared to the new, 'non-planetary' gap in Fig. 11 for the simulation with  $\alpha = 0.001$ 



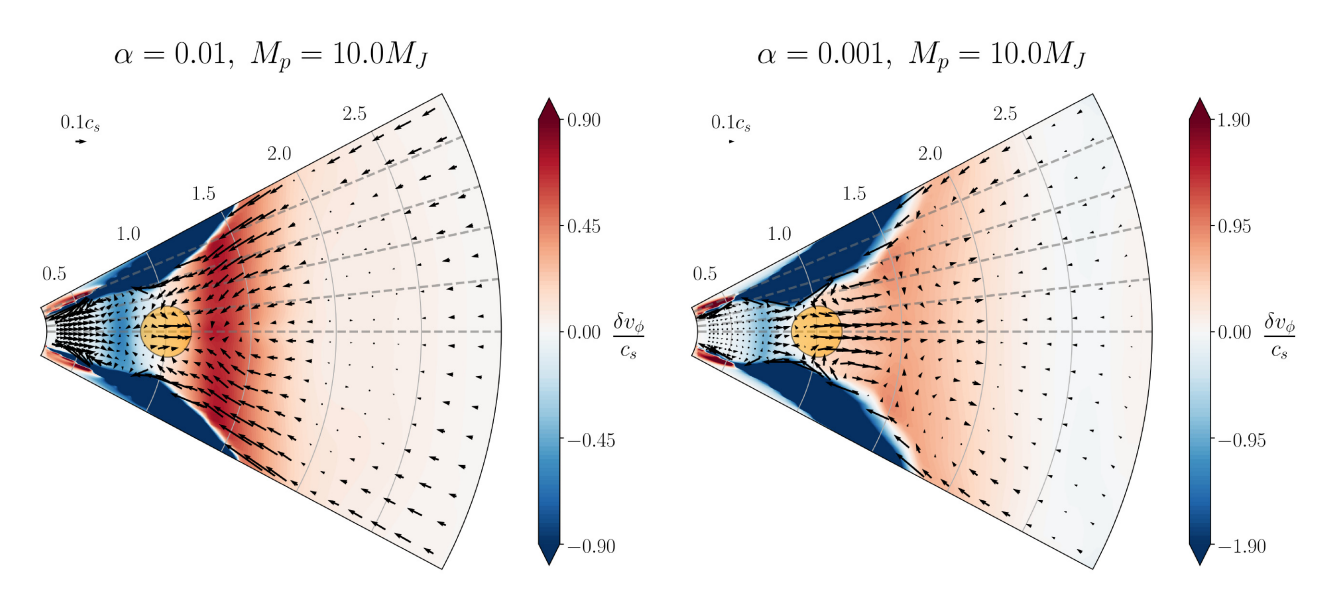
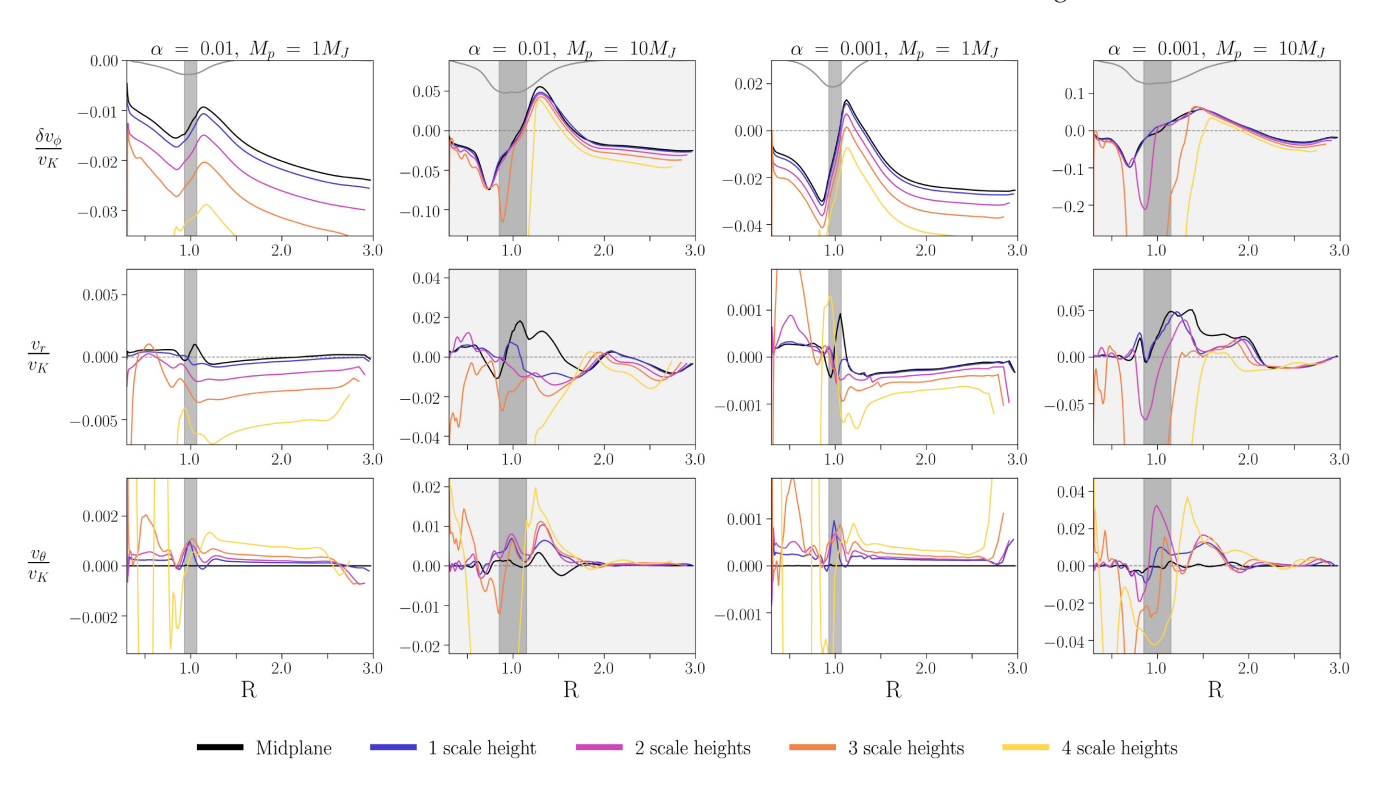


Figure 8. Azimuthally averaged velocity structure for each of the 3D simulations. The black arrows denote the velocity flow in the  $(r, \theta)$  plane. Background colours denote the deviation from normal Keplerian rotational velocity, with red colours indicating super-Keplerian flow and blue colours indicating sub-Keplerian flow. The orange circle denotes the planet's Hill radius. The grey dashed lines mark the disc scale heights. Some vectors are omitted for clarity; see the text for details.

and  $M_p = 1M_J$ . The 'non-planetary' gap is chosen at 10 orbits after removing the planet from the gap. The snapshot of the 'planetary' gap is chosen such that the gap depth  $\Sigma/\Sigma_0$  in both snapshots is nearly the same. Though we only show one simulation in this figure, the behaviour is roughly the same across all of our simulations. The left-hand column shows both 1D and 2D profiles for the planetary gap, while right-hand column shows the same for the non-planetary gap. Comparing the azimuthal velocities, we see that the deviations from normal rotational velocity are nearly identical for both gaps along the full vertical extent of the disc. Thus, a measurement of  $\delta v_{\phi}$  alone is not sufficient evidence to confirm the existence of an embedded planet.

Both the  $v_r$  and  $v_\theta$  components are also similar between the 'planetary' gap and the 'non-planetary' gap with the circulation pattern at the gap edge. The only noticeable difference is that, in the planetary gap, both the  $v_r$  and  $v_\theta$  components at the midplane (black curves) show peaks in the vicinity of the planet's orbital radius. The  $v_r$  peak represents the repelling radial motion away from the planet which is probably driven by the spirals or the gravitational influence of the planet, and the  $v_{\theta}$  peak represents infall on to the planet. Thus these peaks are signatures of the planet itself. However, these signatures are roughly an order of magnitude smaller than the  $\delta v_\phi$  signature, making their detection in velocity maps particularly challenging. Their vertical extent is also quite



**Figure 9.** Azimuthally averaged velocity profiles for the 3D simulations. Each row plots a velocity component versus cylindrical R across multiple scale heights of the disc. Top row: differential azimuthal velocity. The grey curves are surface density curves shown in Fig. 3. Middle row: Radial velocity. Bottom row: Poloidal velocity. All speeds are normalized to the local Keplerian speed. Different colours represent different scale heights in the disc. The shaded regions represent the extent of the planet's Hill radius.

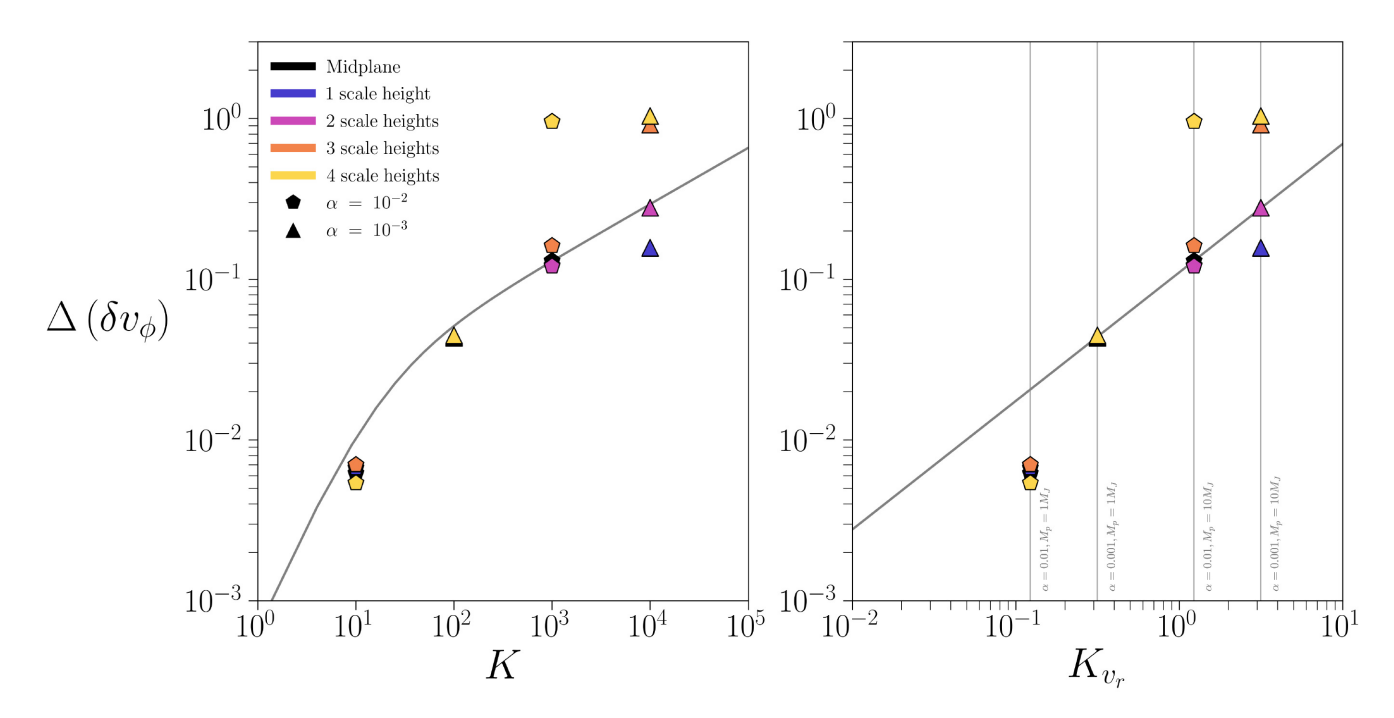
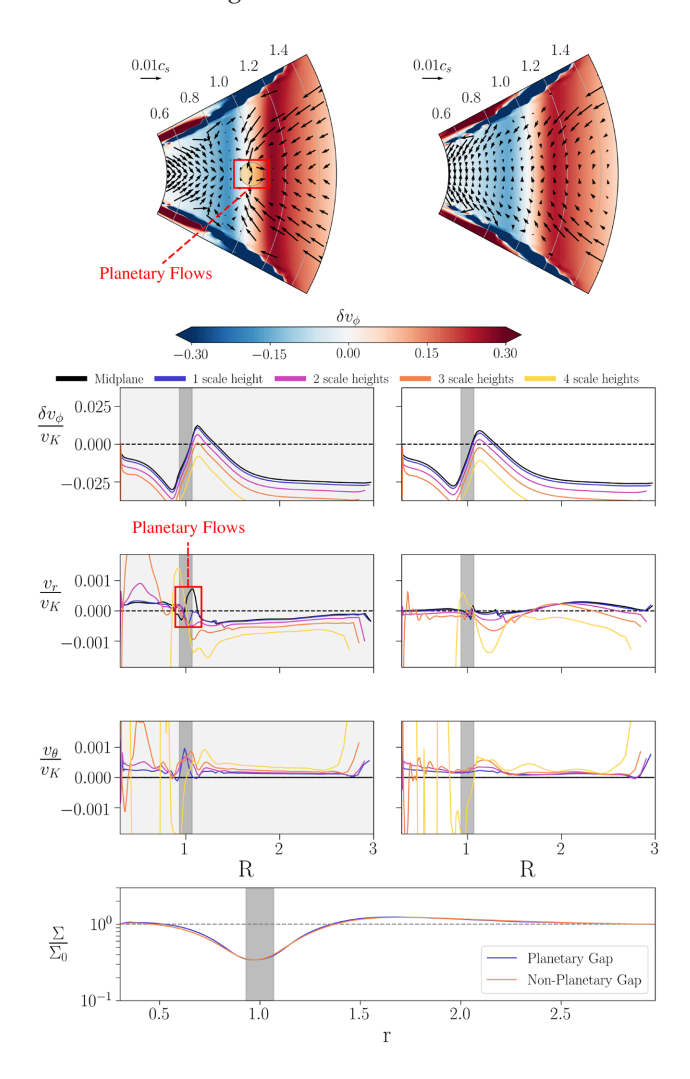


Figure 10. The deviation amplitude  $\Delta(\delta v_{rot})$  plotted for different fitting parameters K. Left-hand panel: Using the fitting parameter from Kanagawa et al. (2015) and best-fitting equation from Gyeol Yun et al. (2019). Right-hand panel: Using the fitting parameter and best-fitting equations from Zhang et al. (2018). Best-fitting equations are shown in grey. Colours are used to represent different scale heights, as in Fig. 9. The triangle and pentagon markers correspond to disc α-viscosities of  $10^{-3}$  and  $10^{-2}$ , respectively, following the convention used in Zhang et al. (2018).



**Figure 11.** Comparison of the disc velocity for 'planetary' and 'non-planetary' gaps in the  $\alpha=0.001$ ,  $M=1M_J$  simulation. Left-hand column: snapshot with a planet opening the gap. Right-hand column: snapshot 10 orbits after removing the planet from the gap. From top to bottom: Azimuthally averaged velocity profile in the  $r-\theta$  plane, zoomed in on r=1; Azimuthally averaged azimuthal, radial, and poloidal velocity components, as presented in Fig. 9; surface density profiles. The snapshots are chosen so that the gap depths for the discs with and without the planet are nearly identical.

limited; the outflows present in the  $v_r$  component weaken quickly with height (disappearing at one scale height), and so are likely not visible with CO measurements. The inflows that cause a signature in the  $v_\theta$  component have a larger vertical extent, of 2–3 scale heights. Another planetary signature which is not captured in our azimuthally averaged approach is the broader line width within the gap due to strong turbulence induced by the planet (Dong, Liu & Fung 2019).

We also compare our constant- $\alpha$  simulations (with  $\alpha=0.001$ ) to our variable- $\alpha$  simulation, which uses the stress profile described by equation (21). Both simulations have  $M_p=1M_J$ . The two models are very similar, with most of the global features remaining the same. The gap in the variable- $\alpha$  model is somewhat shallower than the constant- $\alpha$  model, by a factor of about 1.4. The deviation amplitude in  $\delta v_{\phi}$  is slightly smaller than the constant- $\alpha$  simulation, and so the measured value of  $\Delta(\delta v_{\rm rot})$  would also be smaller. Close to  $z=4H=h_{\rm cut}H$ , the region where the stress profile changes, the gas velocity increases sharply.

## 6 CONCLUSIONS

We have studied how ALMA kinematic observations can help us to constrain (1) the accretion mechanisms, and (2) the planet properties.

We have examined how different disc stress profiles affect its velocity structure, and how the velocity structure in turn affects its subsequent evolution. We find that the radial velocity profile of the disc is very sensitive to the stress profile that is chosen. Thus, future kinematic observations using various molecular lines tracing different disc heights will not only measure the value of  $\alpha$  but also constrain the detailed vertical stress profiles and accretion mechanisms.

On the other hand, as long as the vertically integrated stress is the same, the evolution of the disc's global surface density is unaffected. We also find that steep dropoffs at the outer edge of the disc, which are normally explained by phenomenon external to the disc such as truncation or photoevaporation, can also be explained by a disc with a radially varying  $\alpha$  profile.

In our study of 3D velocity flows of a planet opening a gap in the disc, we are able to see how different velocity components follow different components of the planet–disc system. The radial velocity  $v_r$  traces out the spiral wake of the planet, while the sub-/super-Keplerian velocity  $\delta v_\phi$  traces out the edges of the gap. We observe some dependence of these features on the disc height, especially for massive planet cases which have deep gaps. The linear relationship between the planet mass and the 'kink velocity' is derived, and it is independent from the disc viscosity and the disc height (except for very massive planet cases). Using such a relationship, we predict the 'kink velocity' for the planet candidates in the DSHARP sample.

The velocity deviation at the gap edge within 3 disc scale heights is consistent with previous 2D studies at the mid-plane. We see meridional circulation in the azimuthally averaged velocity maps, and are able to identify components of the circulation process across the vertical extent of the disc. However, by comparing the gap carved by the planet to a gap that is non-planetary in nature, we find that the deviation from Keplerian rotation and the meridional circulation is a feature of the gap and not necessarily a signature of the planet itself. Examining the velocity field throughout the disc reveals some velocity signatures that are unique to the planet, but they are highly non-axisymmetric, limited in their vertical extent, and are an order of magnitude smaller than the deviations caused at the gap edge. Thus, they are not easily detectable in azimuthally averaged velocity maps and may also be difficult to detect with current observations. Combining both axisymmetric kinematic observations and the residual 'kink' velocity is needed to probe young planets in protoplanetary discs. More specifically, we can derive the gaseous gap depth and width using the planet mass constrained by the 'kink' velocity, and then study if the predicted velocity structure at the gap edge are consistent with axisymmetric kinematic observations.

## **ACKNOWLEDGEMENTS**

All simulations are carried out using computers supported by the Texas Advanced Computing Center (TACC) at the University of Texas at Austin through XSEDE grant TG-AST130002 and from the NASA High-End Computing (HEC) program through the NASA Advanced Supercomputing (NAS) Division at Ames Research Center. ZZ acknowledges support from the National Science Foundation under CAREER grant AST-1753168.

## DATA AVAILABILITY

The data used in this paper is available upon request to the corresponding author.

## REFERENCES

ALMA Partnership, 2015, ApJ, 808, L3

Andrews S. M., 2020, Annu. Rev. Astron. Astrophys., 58, 483

Andrews S. M., Wilner D. J., Hughes A. M., Qi C., Dullemond C. P., 2009, ApJ, 700, 1502

Andrews S. M. et al., 2016, ApJ, 820, L40

Andrews S. M. et al., 2018, ApJ, 869, L41

Bae J., Teague R., Zhu Z., 2021, preprint(arXiv: 2102.03899)

Bae J., Zhu Z., Hartmann L., 2017, ApJ, 850, 201

Bai X.-N., 2016, ApJ, 821, 80

Bai X.-N., Stone J. M., 2014, ApJ, 796, 31

Brittain S. D., Najita J. R., Carr J. S., 2019, ApJ, 883, 37

Carrasco-González C. et al., 2019, ApJ, 883, 71

Christiaens V. et al., 2019, MNRAS, 486, 5819

Cugno G. et al., 2019, A&A, 622, A156

Dong R., Rafikov R. R., Stone J. M., Petrovich C., 2011, ApJ, 741, 56

Dong R., Li S., Chiang E., Li H., 2017, ApJ, 843, 127

Dong R., Liu S.-Y., Fung J., 2019, ApJ, 870, 72

Dullemond C. P., Isella A., Andrews S. M., Skobleva I., Dzyurkevich N., 2020, A&A, 633, A137

Espaillat C. et al., 2014, in Beuther H., Klessen R. S., Dullemond C. P., Henning T., eds, Protostars and Planets VI. Univ. Arizona Press, Tucson, AZ, p. 497

Flaherty K. M. et al., 2017, ApJ, 843, 150

Flock M., Turner N. J., Nelson R. P., Lyra W., Manger N., Klahr H., 2020, ApJ, 897, 155

Follette K. B. et al., 2017, AJ, 153, 264

Fromang S., Lyra W., Masset F., 2011, A&A, 534, A107

Fung J., Chiang E., 2016, ApJ, 832, 105

Fung J., Shi J.-M., Chiang E., 2014, ApJ, 782, 88

Fung J., Artymowicz P., Wu Y., 2015, ApJ, 811, 101

Goldreich P., Tremaine S., 1979, ApJ, 233, 857

Goodman J., Rafikov R. R., 2001, ApJ, 552, 793

Gyeol Yun H., Kim W.-T., Bae J., Han C., 2019, ApJ, 884, 142

Haffert S. Y., Bohn A. J., de Boer J., Snellen I. A. G., Brinchmann J., Girard J. H., Keller C. U., Bacon R., 2019, Nat. Astron., 3, 749

Hartmann L., 1998, Cambr. Astrophys. Ser., 32, 38

Hartmann L., Calvet N., Gullbring E., D'Alessio P., 1998, ApJ, 495, 385

Hawley J. F., Gammie C. F., Balbus S. A., 1995, ApJ, 440, 742

Hu X., Zhu Z., Okuzumi S., Bai X.-N., Wang L., Tomida K., Stone J. M., 2019, ApJ, 885, 36

Hu X., Wang L., Okuzumi S., Zhu Z., 2020, preprint (arXiv:2002.01583) Isella A. et al., 2018, ApJ, 869, L49

Isella A., Benisty M., Teague R., Bae J., Keppler M., Facchini S., Pérez L., 2019, ApJ, 879, L25

Jacquet E., 2013, A&A, 551, A75

Johansen A., Youdin A., Klahr H., 2009, ApJ, 697, 1269

Kanagawa K. D., Muto T., Tanaka H., Tanigawa T., Takeuchi T., Tsukagoshi T., Momose M., 2015, ApJ, 806, L15

Keppler M. et al., 2018, A&A, 617, A44

Kley W., Lin D. N. C., 1992, ApJ, 397, 600

Kretke K. A., Lin D. N. C., 2007, ApJ, 664, L55

Lin M.-K., Youdin A. N., 2015, ApJ, 811, 17

Liu H. B., 2019, ApJ, 877, L22

Lubow S. H., Seibert M., Artymowicz P., 1999, ApJ, 526, 1001

Lynden-Bell D., Pringle J. E., 1974, MNRAS, 168, 603

Martin R. G., Lubow S. H., 2011, MNRAS, 413, 1447

Morbidelli A., Szulágyi J., Crida A., Lega E., Bitsch B., Tanigawa T., Kanagawa K., 2014, Icarus, 232, 266

Muto T., Suzuki T. K., Inutsuka S.-I., 2010, ApJ, 724, 448

Nelson R. P., Gressel O., Umurhan O. M., 2013, MNRAS, 435, 2610

Okuzumi S., Momose M., Sirono S.-I., Kobayashi H., Tanaka H., 2016, ApJ, 821, 82

Perez S., Dunhill A., Casassus S., Roman P., Szulágyi J., Flores C., Marino S., Montesinos M., 2015, ApJ, 811, L5

Pérez S., Casassus S., Benítez-Llambay P., 2018, MNRAS, 480, L12

Philippov A. A., Rafikov R. R., 2017, ApJ, 837, 101

Pinte C. et al., 2018, ApJ, 860, L13

Pinte C. et al., 2019, Nat. Astron., 3, 1109

Pinte C. et al., 2020, ApJ, 890, L9

Rameau J. et al., 2017, AJ, 153, 244

Rosotti G. P., Teague R., Dullemond C., Booth R. A., Clarke C. J., 2020, MNRAS, 495, 173

Rozyczka M., Bodenheimer P., Bell K. R., 1994, ApJ, 423, 736

Stoll M. H. R., Kley W., Picogna G., 2017, A&A, 599, L6

Stone J. M., Tomida K., White C. J., Felker K. G., 2020, ApJS, 249, 4

Suriano S. S., Li Z.-Y., Krasnopolsky R., Shang H., 2017, MNRAS, 468, 3850

Szulágyi J., Masset F., Lega E., Crida A., Morbidelli A., Guillot T., 2016, MNRAS, 460, 2853

Takahashi S. Z., Inutsuka S.-I., 2014, ApJ, 794, 55

Takeuchi T., Lin D. N. C., 2002, ApJ, 581, 1344

Tanigawa T., Ohtsuki K., Machida M. N., 2012, ApJ, 747, 47

Teague R., Bae J., Bergin E. A., Birnstiel T., Foreman-Mackey D., 2018, ApJ, 860, L12

Teague R., Bae J., Bergin E. A., 2019, Nature, 574, 378

Tominaga R. T., Takahashi S. Z., Inutsuka S.-I., 2020, ApJ, 900, 182

Urpin V. A., 1984, Sov. Astron., 28, 50

Wagner K. et al., 2018, ApJ, 863, L8

Wang J. J. et al., 2020, AJ, 159, 263

Zhang S. et al., 2018, ApJ, 869, L47

Zhang K., Blake G. A., Bergin E. A., 2015, ApJ, 806, L7

Zhu Z., Stone J. M., 2018, ApJ, 857, 34

Zhu Z., Stone J. M., Rafikov R. R., 2013, ApJ, 768, 143

Zhu Z., Dong R., Stone J. M., Rafikov R. R., 2015, ApJ, 813, 88

Zhu Z. et al., 2019, ApJ, 877, L18

This paper has been typeset from a TEX/LATEX file prepared by the author.